High-Speed Wind Tunnel Tests of a Full-Scale Proprotor on the Tiltrotor Test Rig

C. W. Acree, Jr.
Ames Associate
NASA Ames Research Center
Moffett Field, California, USA

A. L. Sheikman
Aerospace Engineer
NASA Ames Research Center
Moffett Field, California, USA

T. R. Norman
Aerospace Engineer
NASA Ames Research Center
Moffett Field, California, USA

ABSTRACT

The Tiltrotor Test Rig (TTR) is a NASA project, joint with the U.S. Army and Air Force, to develop a new, large-scale proprotor test system for the National Full-Scale Aerodynamics Complex (NFAC). The first wind-tunnel entry was completed in November 2018 with a modern, 26-ft diameter proprotor. The primary purpose was to complete the development of the TTR, including systems integration with the NFAC. The TTR and rotor were tested up to 273 knots in axial flow. This is the highest airspeed ever achieved by a full-scale proprotor in any wind tunnel. Extensive conversion-mode data were also acquired, and hover/climb conditions were explored. Additional testing included aerodynamic tares, motor tests, thermal tests, modal vibration tests, and other checkout activities. This paper summarizes the results of the test, including examples of the most significant data.

NOTATION

BDAS   Basic Data Acquisition System
DCMS   Drive Control Monitoring System
DDAS   Dynamic Data Acquisition System
CFD   Computational Fluid Dynamics
HPP   Half Peak-to-Peak
JVX   Joint Vertical Experimental proprotor
NFAC   National Full-Scale Aerodynamics Complex
RDMS   Rotor Database Management System
SDAS   Steady Data Acquisition System
SOF   Safety of Flight
TTR   Tiltrotor Test Rig
40x80   40- by 80-ft NFAC test section
80x120   80- by 120-ft NFAC test section

A Rotor disk area
c Rotor chord (thrust weighted)
C Wind tunnel cross-section area
C_L Lift coefficient, L/qS
C_P Power coefficient, $P/\rho A V_t^3$
C_T Thrust coefficient, $T/\rho A V_t^2$
D Drag
FM Hover figure of merit, $\left(T\sqrt{T/2\rho A}\right)/P$
L Lift
M_{tip} Tip Mach number
N Number of blades
P Power
P_i Rotor induced power
q Dynamic pressure, $\frac{1}{2}\rho V^2$
R Rotor radius

S Reference area
T Rotor thrust
v Induced velocity
v_h Induced velocity in hover, $\sqrt{T/2\rho A}$
V Wind tunnel airspeed
V' Glauert-corrected airspeed
V_t Rotor tip speed
η Propulsive efficiency, $TV/P = \mu C_T/C_P$
η_c Climb efficiency
μ Advance ratio, V/V_t
Ω Rotor rotation rate
ρ Atmospheric density
σ Rotor solidity, $Nc/\pi R$; or standard deviation
α_1 Area ratio A/C
τ Glauert thrust coefficient, $T/\rho A V^2$

INTRODUCTION

The Tiltrotor Test Rig (TTR) fills a test capability gap for a large-scale proprotor at high-speed axial flight up to 300 knots and tiltrotor conversion mode up to 180 knots. TTR can also test in helicopter mode up to 120 knots. Development of the TTR originated during the U. S. Army Joint Heavy Lift (JHL) effort as a collaborative effort between the Army and NASA. The U. S. Air Force became a partner as the development progressed from design studies to hardware fabrication and testing.

The first entry of the TTR into the National Full-Scale Aerodynamics Complex (NFAC) was completed in November 2018. It was considered a checkout test, where the critical objective was to demonstrate operational safety and efficiency. Every opportunity was used to collect rotor performance and loads data for research. The checkout test used the Model 699 rotor (Fig. 1), which was built specifically

for NASA by Bell and derived from the right-hand rotor of the Leonardo AW609. Testing reached 273 knots maximum airspeed, which is the highest speed ever achieved by a full-scale proprotor in any wind tunnel.

Fig. 1. TTR/699 installed in the (NFAC) 40x80-foot test section (the TTR is oriented at 45° yaw).

The key programmatic objectives of the first entry were prioritized as follows (Ref. 1):

1. Demonstrate the operational capability of the TTR throughout its design flight envelope.
2. Acquire data to support upgrades to the TTR as needed to improve safety and productivity.
3. Acquire benchmark rotor data to determine research capability.
4. Acquire rotor data unique to the 40x80 test section (> 100 knots).

To meet these objectives, research data were acquired over 1500 rotor data points at 60 combinations of rotor rpm, tunnel speed, and yaw angle, plus aerodynamic tares, ground vibration tests, and other supporting data. This paper presents an overview of the entire test, with attention to the unique challenges encountered, such as tare corrections for the large spinner. Performance data are presented for significant test conditions. A separate paper (Ref. 2) presents a correlation study of performance and loads data and predictions, and a third paper (Ref. 3) presents acoustics data. An earlier paper (Ref. 1) describes the development of the TTR, including pre-test activities. Other publications describe the balance calibration (Ref. 4), ground vibration testing (Ref. 5), and pre-test predictions of performance, loads and aeroelastic stability (Refs. 6 and 7).

This report includes descriptions of the TTR, rotor, and test facilities, then presents test data starting at hover/climb conditions, working up in airspeed through the conversion envelope to high-speed axial flow.

SYSTEMS DESCRIPTION

The wind tunnel, test stand, checkout rotor, and auxiliary equipment are described in this section. This section updates and expands on material originally presented in Ref. 1.

NFAC Wind Tunnel

The TTR was designed specifically for operations in the NFAC, which is located at Ames Research Center (Fig. 2) and managed and operated by the U.S. Air Force's Arnold Engineering Development Center.

Fig. 2. National Full-Scale Aerodynamics Complex (NFAC)

The NFAC has two different test sections of different sizes and speed capability (Fig. 3). The TTR/699 checkout test was carried out in the 40- by 80-foot (nominal) test section. In the "40x80" configuration, the wind tunnel is a closed circuit with an oblong test section 39 ft high, 79 ft wide, and 80 ft long. In Fig. 3, the icon representing the TTR and rotor is twice the scale of the rest of the drawing.
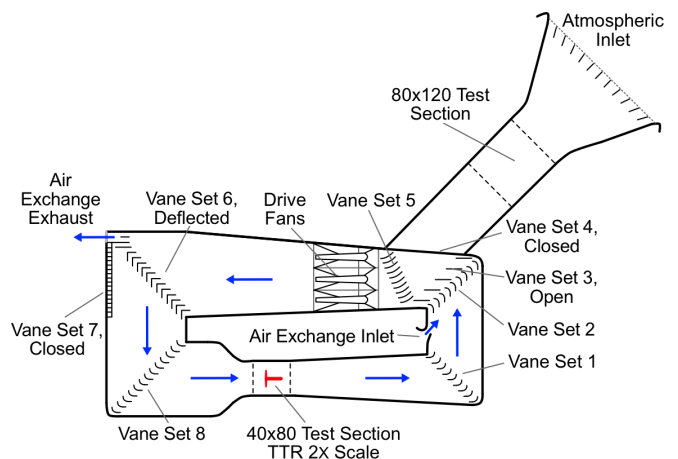

Fig. 3. NFAC high-speed configuration.

The maximum test section velocity is approximately 300 knots (currently limited to about 275 knots, pending upgrades

to the fan drives). The tunnel walls are treated with 42 in of acoustically absorbent material to reduce reflections that can contaminate the noise field. The NFAC overhead doors were closed for all TTR tests, whereas they were sometimes open during previous proprotor hover tests (Refs. 8 and 9).

The NFAC can be internally reconfigured as an open-circuit tunnel with an 80- by 120-ft rectangular test section. The TTR can be tested in the "80x120", although at much lower air-speed (about 100 knots maximum). For certain hover tests, the NFAC was set up in a non-standard configuration, discussed in the Hover (Vertical Climb) Data section.

TTR Technical Details

Table 1 summarizes the dimensions and technical features of the TTR with the 699 rotor installed. The airspeed limits apply to the TTR under ideal conditions; wind-tunnel operations are limited by dynamic pressure, not velocity. Aircraft nacelle tilt is simulated by yawing the TTR in the test section. Zero deg yaw is airplane mode, with the rotor pointing into the wind, and 90 deg yaw is helicopter mode, with the rotor edgewise to the flow. Figure 1 shows the TTR at 45 deg yaw.

The TTR has a three-strut layout to interface with the test section turntable (Fig. 1). The mounting struts attach directly to the test section T-frame, a rotating structure underneath the floating turntable. The T-frame was modified to rotate ±180 deg from its normal orientation to accommodate the TTR. The large overhang between the single forward strut and the rotor provides space for a semi-span wing, as would be needed for wing/rotor interference measurements.

No strut fairings were installed for the checkout test. The bare struts lowered maximum airspeed, but simplified mainte-nance. The tradeoff was considered acceptable for the first entry.

Table 1. TTR Dimensions and Design Capabilities

Length, including spinner	435 in
Width, main nacelle only	85 in
Width, including pylons	140 in
Depth, main nacelle only	67 in
Weight, including rotor	60,800 lb
Rotor hub position:	
forward of balance center	88 in
height above floor (40x80)	234 in
Power, max design	6,000 hp
Power, max (30 min)	5,500 hp
Power, continuous (2 hr)	5,000 hp
Rotor shaft speed, max	629.5 rpm
Max airspeed, 0 deg yaw	300 knots (305 lb/ft^2)*
Max airspeed, 90 deg yaw	180 knots (110 lb/ft^2)*

*40x80 limit=262 lb/ft^2, 80x120 limit=33 lb/ft^2

Rotor forces and moments are measured by a dedicated balance installed between the gearbox and the rotor. Rotor torque is measured by an instrumented torque tube inside the gearbox. Table 2 summarizes the capability of the current balance. The TTR structure is sized for even higher loads: ±20,000 lb shear, ±90,000 ft-lb hub moment, and 75,000 ft-lb torque. This load range is intended for proprotor hubs with substantial hub moments, based on emerging new tiltrotor concepts. The calibrated capability of the balance is described in the Rotor Loads Measurement section.

Table 2. Rotor Balance Capability (maximum range)

Load (applied at the rotor hub)	Limit
Normal force (thrust), lb	30,000
In-plane shear, lb	±10,000
Hub moment, ft-lb	±60,000
Torque, ft-lb	72,000
Actuator loads, lb	±11,000

Figure 4 shows the TTR main deck with upper cowlings open. The large cylinders are the drive motors; the various boxes are all electronics cabinets. The aft end of the gearbox is just visible under the cowling on the right-hand side of Fig. 4.

Fig. 4. TTR main deck: drive motors and electronics.

The water-cooled, AC induction motors are intended to be powered in pairs by two NFAC motor-generator sets, rated up to 150 Hz, or 3000 rpm nominal, and 1100 volts. The motors were surplus units refurbished and upgraded to TTR requirements. The drive motors are presently rated to 5000 hp total continuous power—enough to drive proprotors more capable than any currently in existence at this scale. Only one pair of motors was powered during testing of the checkout rotor. The drive train was designed to allow operation down to 20% of maximum shaft speed Ω at full torque (hence maximum power reduces with Ω).

The TTR gearbox and drive train are sized for 6000 hp. The maximum power actually achieved during the checkout test was just under 1000 hp per motor at 569 rpm output shaft speed (the maximum Model 699 rotor shaft speed). Exact speed and torque varied with air temperature. The four motors are theoretically capable of greater power, but will require testing with a different rotor or other torque generator to determine the actual value.

Control of motor, gearbox and mast module temperatures was an important concern during development of the TTR and required adjustments to the thermal control system. All temperatures were well-controlled throughout the test.

To facilitate testing different rotors, TTR has a multi-component drive train. The rotor mast has splined fittings at each end, connecting to the rotor hub at the forward end, and into a hollow drive shaft at the aft end. Installing a different rotor usually requires a different hub, hence a different rotor mast. If the mast were an integral part of the drive train, a new rotor would require a new drive train, including a modified gearbox. This arrangement allows the rotor mast and hub to be removed and replaced without disassembling the rest of the drive train or disturbing the balance or gearbox. The mast module contains the bearings that support the drive shaft and rotor mast. The various components of this system are briefly described here.

The forward end of the TTR—from the gearbox bulkhead to the rotor instrumentation module ("hat")—is shown in Fig. 5, here without cowlings, spinner or pitch links. Internal components are shown in Fig. 6. The rotor balance attaches directly to the TTR main bulkhead, and the mast module and control actuators (the white tubes in the photo) attach to the forward end of the balance. A swashplate support tube attaches to the forward end of the mast module. A torque tube, gear coupling, drive shaft, and rotor mast all run through the center of the balance/mast-module/support-tube assembly. All rotor instrumentation is routed through the spinner to the hollow rotor mast, connecting to a slip ring behind the gearbox.

Checkout Test Rotor

The checkout test used the Bell Model 699 rotor, derived from the Leonardo AW609 rotor. Although built in the same blade molds as the production rotor, the checkout rotor is unique: it has no deicing or pendulum absorbers, and has special instrumentation and modified controls as appropriate for a wind-tunnel test article. The pitch horn lugs are inverted to connect to the TTR control system. These modifications prevent the rotor from ever being flown on an aircraft.

Figure 7 is an exploded view of the spinner, hub, and one blade. Table 3 summarizes the rotor characteristics.

The rotor is a stiff-in-plane design with a gimballed hub; there are no discrete flap or lag hinges. The hub is mounted to the rotor mast by a gimbal (Fig. 7), so that all blades flap together: if one quadrant flaps up, the opposite flaps down. The gimbal is a constant-velocity (CV) joint and includes a flapping spring. The hub spring and rotor bearings are all elastomeric units.
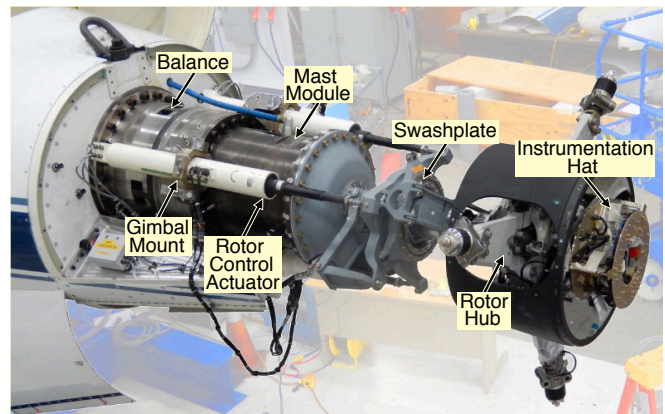

Fig. 5. TTR forward end: rotor balance, mast module, controls, hub and skirt fairings.
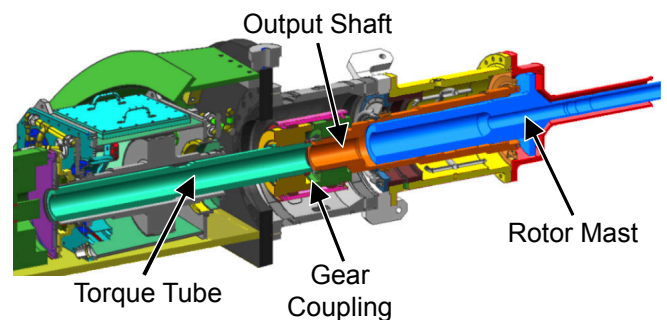

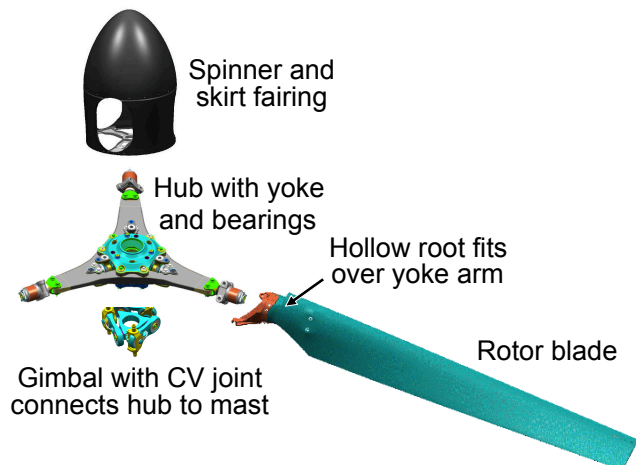**Fig. 6. TTR drive train internal components.**

Fig. 7. Checkout rotor exploded view (components not to scale).

The rotor blades have hollow roots that slip over the yokes and bearings. The entire hub, including pitch links, pitch horns, and blade roots, is covered by a spinner and side panels, or skirts, all of which rotate together. The skirts have oversize cutouts to allow for blade flapping.

Table 3. TTR Checkout Rotor Characteristics

Number of blades	3
Diameter	26.0 ft
Disc area (per rotor)	530.9 ft^2
Solidity (thrust weighted)	0.0908
Blade chord (thrust weighted)	14.83 in
Blade area (per rotor)	48.2 ft^2
Blade twist (non-linear)	47.5 deg
Blade taper ratio (linear)	0.684
Blade tip shape	square
100% rotor speed (helicopter mode)	569 rpm
Tip speed	775 ft/sec
84% rotor speed (airplane mode)	478 rpm
Tip speed	651 ft/sec
Gimbal limit (flapping stop)	±11 deg
Precone	2.75 deg
Undersling	0.36 in
Delta-3, maximum (pitch horns level)	−15 deg
Direction of rotation (looking aft)*	CCW

*As installed on TTR.

Control Systems

The TTR rotor control system uses a conventional rise-and-fall swashplate, here driven by three long-stroke, dual-motor, electric jackscrew actuators. Maximum actuator travel is 17 in, equivalent to 61.5 deg of blade pitch for the checkout rotor. The large amount of pitch motion is required for a proprotor that must operate over an extremely large range of inflow velocities (0-300 knots).

The actuators are controlled by a pair of identical control consoles that provide fully redundant backup in case of failure. Each console has a set of conventional collective and cyclic controls, plus individual actuator controls. Each console has a pair of displays with critical rotor information.

A companion console, the Drive Control Monitoring System (DCMS), controls essentially everything on the TTR except the rotor itself. The DCMS controls and monitors only low-rate systems. The rotor can be safely flown down from full speed and power to a stop even after a complete failure of the DCMS. Controls for the NFAC motor-generators (M-G sets) that drive the motors are co-located with the DCMS.

The rotor control consoles and DCMS are completely independent of the NFAC data system, although the two systems can exchange data.

Instrumentation

Table 4 summarizes the instrumentation currently installed on the TTR and checkout rotor. A few measurement categories unique to the TTR are discussed below. The rotor balance is discussed in a separate subsection, Rotor Loads Measurement. In addition, the NFAC data system acquires a comprehensive set of wind tunnel test conditions, including yaw angle, airspeed, temperature, density, static pressure, etc.

Tables 5 through 9 give more details of the TTR instrumentation. The tables are organized as traditional rotating and nonrotating sensors, with additional details for blade strain gages, the rotor balance system, and external microphones. A few categories overlap; e.g., the torque tube is in Tables 5 and 8.

Table 4. TTR/699 Instrumentation Summary

76 Rotating Channels:
Blade and yoke strain gages
Hub flap, blade pitch
Pitch link loads
Mast torque and bending
Elastomeric bearing temperatures
Spinner loads
Torque-tube loads and temperatures
88 Fixed Channels:
Control positions & loads
Swashplate guide tube bending
Rotor balance loads and temperatures
Strut loads
Microphones
On-board utilities (non-research data)

Table 5. Rotating System Instrumentation

Strain gages	
Blade loads	12 (5 locations)
Yoke & spindles[a]	8 (4 locations)
Pitch links	3
Swashplate & driver	2
Mast torque[b]	3 (2 locations)
Mast bending	6 (2 axes at 3 locations)
Torque tube	8
Diaphragm coupling	2
Spinner	12 (4 locations)
Angles	
Hub flap angle	2 axes
Blade pitch angle	2 blades
Temperatures	
Swashplate	2
Hub spring	4
CF bearing	2 blades
Torque tube & diaphragm	4
Other	
Hub accelerometers[c]	3
Hub pressure[c]	1

[a]One yoke arm and its bearing spindles have beam and chord gages at two locations each.
[b]Mast torque has a backup gage at only one location.
[c]The hub accelerometers and pressure sensor are mounted to the instrumentation "hat", which does not flap with the hub.

Table 6. Blade Strain Gages

Station	Beam	Chord	Torsion
0.21 R	x	x	
0.37 R	x	x	
0.45 R	x	x	x
0.58 R	x	x	
0.75 R	x	x	x

Table 7. Nonrotating System Instrumentation

Rotor balance system (all sensors)	56
Control actuator loads	3
Control actuator positions[a]	6
Swashplate anti-drive load	1
Swashplate support tube strain gages	2
Shaft encoders (4096/rev)	2
Mast module pressure	1
Support strut strain gages[b]	12
Microphones	4

[a]Each actuator has primary and backup transducers.
[b]Each strut has two pairs of transverse strain gages (primary and backup).

Rotor Loads Measurement

The TTR has a balance and torque tube that work together to measure rotor loads (Table 8). The balance measures all rotor and actuator loads except torque, which is measured by the torque tube. The torque tube connects to the output shaft via a gear coupling that transfers only torque, isolating the torque tube from bending and thrust loads. The torque tube has a diaphragm coupling to relieve stresses arising from thermal expansion.

Table 8. Balance & Torque Tube

Balance strain gages	24
Balance temperatures	24
Torque tube strain gages	2
Torque tube temperatures	2
Diaphragm coupling strain gages	2
Diaphragm coupling temperatures	2

The balance is a metal cylinder fixed to the gearbox bulkhead. Rotor loads are transferred to the balance via thrust bearings inside the mast module. For accurate measurement, loads are concentrated at four machined posts, each with two sets — primary and backup — of three strain gages (axial, side, and normal). The balance has thermal isolation rings and a temperature control system, including pre-heating, with metric and ground temperature sensors every 45 deg.

The torque tube has strain gages mounted to a necked section for high sensitivity. The diaphragm coupling also has strain gages to measure any residual thrust. The torque tube and diaphragm coupling have primary and secondary (backup) measurements.

For a proprotor at high speed, control loads can be a very large component of total thrust, so care must be taken to measure such loads. The control actuators mount to the TTR via gimbals (Fig. 5), which transmit only axial loads from the rotor. The gimbals in turn mount directly to the metric side of the balance, so that the balance measures the sum of rotor thrust through the rotor mast and control loads through the actuators. The control actuators (nonrotating) and pitch links (rotating) have calibrated strain gages to measure control loads.

Rotor Balance

The rotor loads measurement system is commonly referred to as the "rotor balance", or just "balance". The name derives from traditional wind-tunnel scales that balance loads being measured against known weights. TTR does everything electronically, but honors the traditional name. The entire system, including balance and torque tube, was calibrated when installed on the TTR. Calibration procedures are described in Refs. 1 and 4; the results are summarized here.

The TTR rotor balance is overdesigned for the checkout rotor. The rotor has a gimballed hub, so it cannot sustain large moments. Calibration was therefore conducted over two load ranges: the full load range of the rotor balance (Table 2), and the load range for the checkout rotor (Table 9). The checkout rotor has a maximum thrust just over 1/2 of the balance range, maximum hub moments 1/8 of the balance range, and maximum torque less than 1/3 of the torque tube range.

For a proprotor, the ratio of thrust in cruise to that in hover is approximately the inverse of the aircraft lift-to-drag ratio, yet the torque can be equally high. Hence thrust can vary by an order of magnitude depending on flight condition. The balance must be sized for hover loads, which results in thrust having reduced accuracy relative to loads in cruise.

Table 9 summarizes the calibration accuracy for the best set of calibration equations derived to date. (Table 9 has been updated subsequent to Ref. 1, with all values here referenced to the rotor hub.)

Torque and in-plane load accuracies are good at 0.42% range or less. However, thrust accuracy is 0.80% of range. The result for thrust is disappointing but not surprising, given that the rotor balance is working over barely 50% of its design range. Hub moment accuracies are worse in terms of % range, largely because the calibration was matched to the 699 rotor, and not to the full range of Table 2.

To compute balance loads, the voltages from the balance strain gages are summed and differenced as appropriate for each force and moment, then calibration coefficients are applied to the combined voltages. The primary set of gages is used for all data reported here. For reference, this combination of gages and coefficients is labeled "B3" in the database.

Table 9. Rotor Balance Calibration for Checkout Rotor Loads

Hub Load	Range	2σ Error	2σ/Range
Normal force (thrust)	15,148 lb	120 lb	0.80 %
In-plane horizontal	±8,250 lb	24 lb	0.15 %
In-plane vertical	±8,250 lb	18 lb	0.11 %
Hub moment, vertical axis	±7,500 ft-lb	175 ft-lb	1.16 %
Hub moment, horizontal	±7,500 ft-lb	225 ft-lb	1.50 %
Torque	22,338 ft-lb	93 ft-lb	0.42 %

Data Streams and Storage

Rotor research data are cooperatively processed by NFAC and NASA data systems. The NFAC acquires the data, including basic sampling and filtering, and provides real-time displays of critical operational and Safety of Flight (SOF) data (Ref. 10). The NASA Rotor Database Management System (RDMS) performs post-run data processing, including per-revolution windowing and resampling; computes filtered time histories, derived parameters, statistics, and spectra; and stores the data in a network-accessible database.

TTR data acquisition has five different data streams, summarized here in order of decreasing sample rate. Acoustics data are acquired by the Dynamic Data Acquisition System (DDAS). Signals from the microphones (visible at the lower right in Fig. 1) are sampled by fixed frequency (65,536 s/s) analog-to-digital converters (A/Ds), then digitally resampled to synchronize with rotor azimuth. A 4096/rev shaft encoder provides the synchronization signal. The acoustics data are stored at 2048/rev (>19 kHz at 569 rpm).

The great majority of research data includes inputs from fixed and rotating TTR instrumentation. The combined data stream is managed by the Basic Data Acquisition System (BDAS). Fixed-system TTR data include control positions and the rotor balance. Rotating-system signals pass through a conventional analog slip ring, then to the NFAC data system. The TTR data are initially sampled by the same method as the acoustics data, but resampled at 256/rev and processed to generate a variety of derived parameters and statistics for each data point. Processing includes computation of balance loads from strain gage signals, rotor coefficients, etc. Typically, 128 revolutions of data are stored for each data point.

A subset of the rotor and balance data are acquired and processed separately for Safety of Flight (SOF) monitoring on real-time displays. To maximize robustness and minimize time lags, the SOF data stream uses its own set of A/Ds and does not synchronize with the rotor. Such data are sampled at 2,000 s/s and only simple processing is allowed. The SofDAS data are not normally stored in the database because the BDAS data are more time-accurate and have more extensive processing.

Some data vary little during a given data point and are acquired at very low sample rates (<10 Hz). Such data include TTR balance temperatures and NFAC test section instrumentation (airspeed, density, etc.). These data are managed by the Steady DAS (SDAS) with minimal processing and are stored as constant values for each rotor revolution.

A separate, on-board system manages low-rate utility data, such as cooling water temperature, lubrication oil, and balance temperature. This data stream primarily feeds the rotor operator displays and controls (DCMS and control console). Most such data are not needed for research and are not normally stored in the database.

It is possible to cross-feed data between streams via "virtual" data channels, although TTR makes very limited use of this capability. Data intended for permanent storage—the DDAS, BDAS and SDAS data streams—are processed and stored by the NASA RDMS. Summarizing, DDAS data are stored at 2048/rev, BDAS data at 256/rev, and SDAS data as constant values for each revolution.

TEST ACTIVITIES

Rotor research objectives of the first entry (Ref. 1) are given in order of testing:

1. Fully characterize hub/spinner drag
2. Hover up to rotor thrust limit (stall)
3. Airplane mode (axial flow) up to maximum tunnel speed
4. Helicopter mode (edgewise flow) up to 120 knots
5. Conversion mode up to 180 knots

Although not all of these objectives were met to the letter, more than enough data were collected to satisfy the intent. Hover and conversion-mode limits were often determined by control system loads, not true blade stall, and high-speed helicopter-mode conditions (>60 knots) were deprioritized in favor of acoustics data. The maximum airspeed in airplane mode was determined by temporary load limits on the NFAC fan drives.

Supporting Tests

The most important pre-entry test activity was the rotor balance calibration; see Refs. 1 and 4. The first test done upon installation into the NFAC was a ground vibration test (Ref. 5). Wind-on testing began with tare measurements. The great majority of subsequent testing was envelope expansion

combined with rotor performance measurement, discussed in separate sections for hover/climb, conversion mode, and airplane mode.

In addition, there were thermal tests comprising diagnostic temperature measurements within the TTR drive train and rotor balance. The drive train temperatures remained within limits, thus verifying the performance of the thermal control system. As of this writing, the rotor balance temperature data are being analyzed. It is expected that the results can be used to adjust the balance strain-gage data, thereby improving the accuracy of the rotor loads measurements.

During development of the TTR, there was no readily available facility that could bench test the drive motors to full speed and torque at rated voltage, current, and frequency. The TTR itself is the means of qualifying the motors to full power. Motor testing was therefore an important part of the first entry and a good example of the unique challenges faced by TTR development.

For such tests, only one motor at a time was connected to the NFAC motor-generator set while the TTR and test section were configured for hover operations. Motor voltage, current, torque, and internal temperature were monitored as rotor thrust was increased. Where possible, the motor tests were combined with hover research runs. The results of these tests were summarized above in the section TTR Technical Details.

Test Limitations

The TTR control system combines components from production aircraft (not necessarily the 609), modified aircraft parts, and parts unique to the TTR. The combination did not always work well in the wind-tunnel environment, where the rotor can be operated under conditions not reachable in flight, sometimes for extended periods. The resulting high internal control loads sometimes limited achievable test conditions. Such loads are unique to TTR and are not true rotor limits.

In addition, thrust or airspeed was sometimes limited by internal hub loads, when TTR operating conditions went beyond the limits of trimmed flight for the aircraft.

The maximum airspeed was determined by load limits on the NFAC, and true hover (zero airspeed) is not achievable in the 40x80 test section. The NFAC also has a minimum airspeed when the fan drives are directly connected to power ("utility mode"). In the 40x80 test section, the minimum wind-on airspeed was about 57 knots, depending on temperature. Lower speeds are possible, but require time-consuming reconfiguration of fan drive power. Very low wind-on airspeeds were not a TTR test priority, so the 57-knot limit was completely acceptable.

Summing up, maximum achievable thrust, torque, or airspeed could be restricted by any of several factors: TTR control loads, TTR aerodynamic loads, NFAC power limits, NFAC load limits, hub loads, or blade loads. Note that only the last

two are true rotor limits; the rest do not apply to any production rotor, and even the rotor limits may not be relevant to aircraft operations. See the section "Future Work" for a discussion of improvements to these limitations.

ROTOR DATA

The following sections summarize the rotor data acquired, with emphasis on performance data. Blade loads are discussed in Ref. 2, and acoustics data are discussed in Ref. 3.

Test Envelope and Trim Procedures

Reference 11 gives details of the checkout rotor's flight envelope, from which the wind tunnel test conditions were derived. Figure 8 summarizes the rotor operating limits in conversion mode, overlaid with test points at which thrust sweeps were taken. To avoid distorting the scale, airplane-mode data are shown only up to 200 knots. The aircraft can exceed the nominal limits on the high side, at least transiently, and the TTR can exceed the limits on the low side (there being no need to trim the aircraft). The data taken during the checkout test were more than adequate to verify the design capability of the TTR.
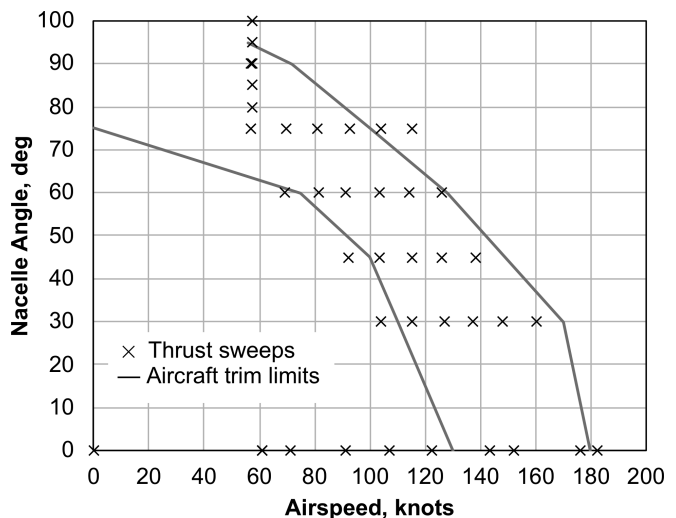

Fig. 8. Nominal conversion-mode envelope and test conditions.

The rotor can be flown at low speeds with a slight negative tilt angle, useful for descent to landing, so the figure contains a few test points to simulate such flight conditions. In a wind tunnel, there is no need to trim the complete aircraft, so the boundaries of Fig. 8 are not necessarily definitive for an isolated rotor on the TTR.

Not shown in Fig. 8 are acoustics data points at 58 knots (μ=0.125) taken over very fine variations of yaw angle; see Ref. 3 for discussion. Also not shown are aerodynamic tare data points, discussed in the section Conversion-Mode Data.

In the wind tunnel, the rotor is trimmed to M_{tip} and μ, not rpm and velocity, so the actual airspeed varies with wind tunnel temperature. Close examination of Fig. 8 shows that the data

points do not always line up perfectly on a given airspeed, which is intentional.

Following standard NFAC practice, the rotor was trimmed to zero flapping for all performance data points. Control-sensitivity data points (not included here) were set to ±1 deg cyclic control variations from zero-flapping trim. In such cases, rotor flapping was a fallout, not a trim target.

In traditional wind-tunnel coordinates, 0 deg yaw equals −90 deg rotor angle of attack, and 90 deg yaw equals 0 deg angle of attack. This equivalency holds only for zero flapping. The TTR/699 database includes standard NFAC wall-effect corrections for aerodynamic angle of attack. All data shown here are referenced to geometric rotor yaw angle, without any correction for wall effects.

Hover (Vertical Climb) Data

In the NFAC, true hover (wind off) is challenging at full scale. The effects of tunnel walls cannot be completely avoided in the 40x80 test section. Furthermore, the rotor's induced velocity continues around the tunnel circuit without completely dissipating, so the test conditions are actually low-speed vertical climb.

The NFAC can be configured to operate as either a closed-circuit tunnel, intended for high-speed testing in the 40x80 test section, or as an open circuit tunnel using the 80x120 test section, necessarily at lower airspeed. Various vane sets, vents and louvers (Fig. 3) are adjusted to accommodate the different internal airflows. Furthermore, the TTR can be rotated on the T-frame to face either upstream or downstream.

During the hover tests, eight different combinations of tunnel configurations were tested to determine their effects on hover performance. When comparing the resulting rotor data, a tradeoff must be made between maximum thrust, minimum tunnel velocity, and unsteady loads.

Track and balance runs and motor tests also produced limited but useful hover data. For example, Ref. 2 reports load variations for varying rotor speed Ω at fixed collective. In contrast, the data reported here were taken at fixed Ω and varying collective.

A subset of the hover/climb data runs is shown here, selected to best reveal the similarities and differences between configurations. Runs 61 and 62 used the 40x80 configuration (Fig. 3), whereas Runs 63 and 110 had Vane Sets 6 and 7 in the 80x120 configuration (Vane Set 6 straight and Vane Set 7 open). The rotor was set to 0 deg yaw for Runs 61 and 110, and to 180 deg yaw for runs 62 and 63.

Figs. 9-14 plot the most complete thrust sweeps for the rotor at 0 deg and 180 deg yaw (upstream and downstream orientation, respectively). It is evident from Fig. 9 that the upstream orientation requires higher power for any given value of thrust, and that the TTR orientation makes a larger difference than other changes to the flow path.
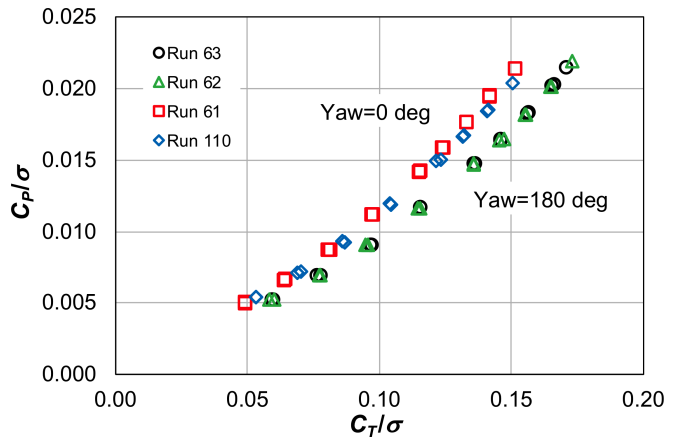

Fig. 9. Selected hover/climb data, 0 deg vs. 180 deg yaw, M_{tip}=0.684.

Figure 10 explains the difference: test-section airspeed is plotted against thrust. Here, airspeed is referenced to the rotor, hence always positive. The wind-tunnel velocity induced by the rotor is higher at 0 deg yaw, so the rotor is operating at an effectively higher vertical rate of climb. The Glauert airspeed correction (discussed below) reduces the equivalent airspeed slightly at 0 deg yaw and high thrust, but has negligible effect at 180 deg yaw. The Glauert correction is not normally applied to the test-section airspeed data, so it is not included in Fig. 10; it does not change the interpretation of the results in this case.
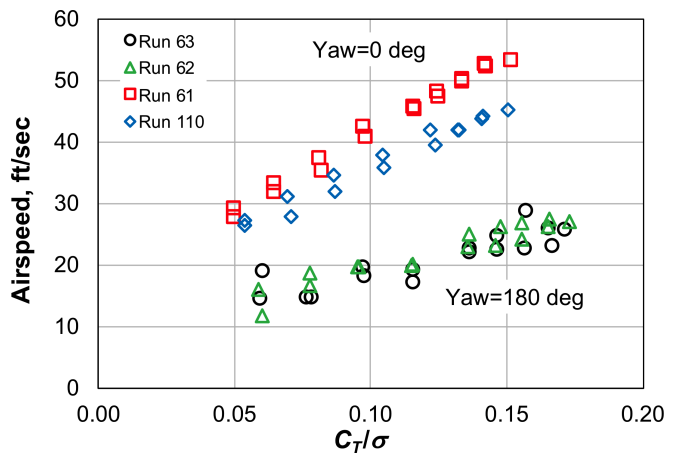

Fig. 10. Rotor-induced test section airspeed, 0 deg vs. 180 deg yaw, M_{tip}=0.684.

A consequence of orientation is a large increase in unsteady loads at 180 deg yaw. Figure 11 plots unsteady thrust as ½ peak-to-peak load (HPP) vs. average thrust. Run 61 had the lowest unsteady loads, whereas Run 62 usually had the highest loads. Runs 61 and 62 both had the vane sets in the high-speed configuration, and the only difference was the rotor orientation. The other configurations had intermediate values of power and unsteady loads vs. thrust.

9

Opening Vane Set 7 slightly reduced the tunnel airspeed (Run 110, Fig. 10), but it also slightly increased the unsteady loads (Fig. 11). Attempts were made to further reduce airspeed and loads by operating with Vane Set 4 open to the 80x120 test section (Fig. 3). Those tests did not result in discernable improvements, so their data are not shown here.

No judgement is offered here as to the "best" hover data. The researcher must make a tradeoff between maximum thrust, minimum induced flow, and unsteady loads, as appropriate to the nature of the research being undertaken.
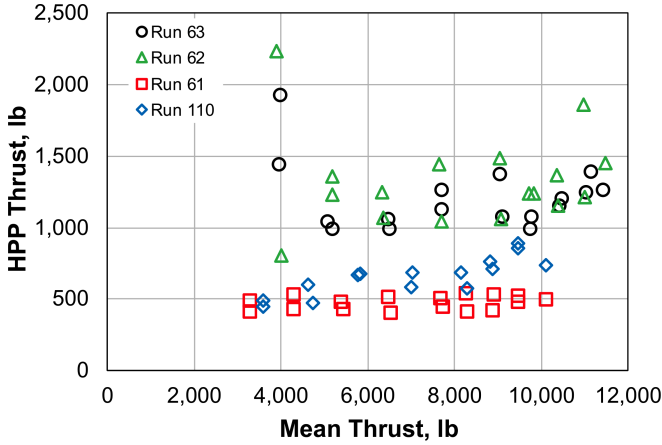
Fig. 11. Unsteady thrust loads, 0 deg vs. 180 deg yaw, M_{tip}=0.684.

Efficiency Metric

Neither figure of merit nor propulsive efficiency are appropriate for the operating conditions discussed here. Reference 12 suggests a generalized rotor efficiency derived from the momentum theory result for ideal power in axial flow:

$$P_i = T(V + v) = T(V/2 + \sqrt{(V/2)^2 + v_h^2}) \qquad (1)$$

$$v_h = \sqrt{T/2\rho A} \qquad (2)$$

Where P_i = ideal power, T = thrust, V = airspeed, A = rotor disk area, ρ = density, v = induced velocity, and v_h = induced velocity in hover.

We can define climb efficiency $\eta_c = P_i/P$, where P is measured power. As $V \rightarrow 0$, η_c becomes the traditional rotor figure of merit, and for $V \gg v$, η_c approaches the traditional propeller propulsive efficiency.

Figure 12 plots climb efficiency vs. thrust. The results no longer fall into clearly separate bands, although the data at 0 deg yaw (Runs 61 and 110) show less scatter than that at 180 deg yaw (Runs 62 and 63).
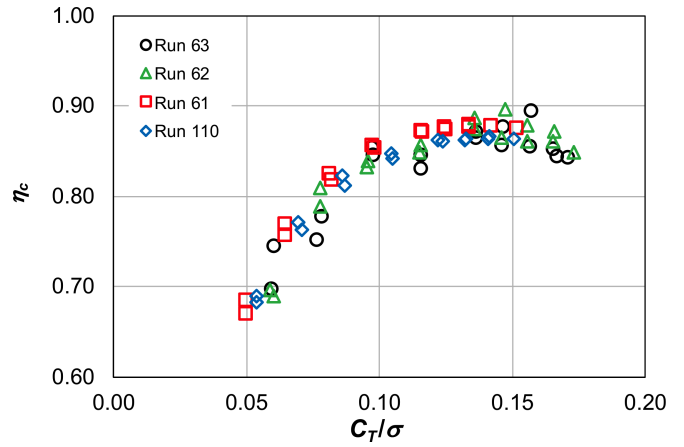
Fig. 12. Climb efficiency η_c for nominal airspeed, M_{tip}=0.684.

There are two potential problems with this evaluation of rotor efficiency. First, measurement of low values of airspeed is problematic, particularly in reverse flow through the test section at 180 deg yaw. The standard NFAC data system measured airspeed upstream of the rotor at 0 deg yaw, but downstream at 180 deg yaw, hence the measured airspeed for 180 deg yaw is probably too high.

Second, the airspeed measured in the wind tunnel is not perfectly representative of that experienced by the rotor in free flight. The second problem is addressed here by the Glauert correction. The method used here was originally developed by Glauert (Ref. 13); the equations below are taken from Ref. 14.

In the wind tunnel, the influence of the test section walls changes the flow conditions at the rotor disk relative to what would exist in free-stream flow (that is, with an infinitely large wind tunnel). The Glauert correction derives an equivalent free-stream velocity V' at which the rotor will experience the same axial velocity as in the wind tunnel, and for which "this condition will maintain the same working conditions for the airscrew blades" (Ref. 13).

Let $\tau = T/\rho A V^2$, and $\alpha_1 = A/C$, where C = wind tunnel cross-section area. The Glauert correction is then

$$V'/V = 1 - \tau \alpha_1/(2\sqrt{1 + 2\tau}) \qquad (3)$$

V'/V is here calculated using a literal interpretation of the Glauert formula, with no allowance made for the wind tunnel's non-circular cross section or boundary layer, nor with any other blockage correction, such as for the TTR's large afterbody. Substituting V' into equation (1) and recalculating yields η_c', the Glauert-corrected climb efficiency, plotted in Fig. 13.

The Glauert correction reduces the climb efficiency by a few percent (compare Figs. 12 and 13). In this report, the correction is applied only to pure axial flow. While a more

sophisticated method would be useful, equation (3) has the virtue of simplicity and is easily applied within the RDMS database or a spreadsheet. The simple correction used here is sufficient to show that the Glauert effect applies even to low-speed vertical climb conditions. It is recommended to use the Glauert correction (or higher order) when comparing these results to flight-test data or other wind-tunnel data.
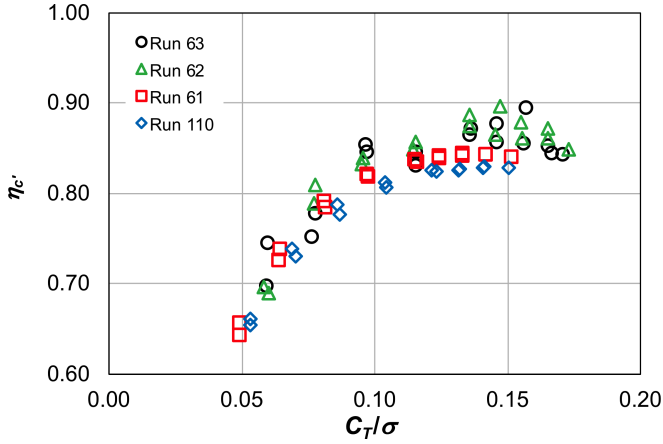

Fig. 13. Glauert-corrected climb efficiency η_c', M_{tip}=0.684.

For the sake of completeness, traditional figure of merit $FM = \left(T\sqrt{T/2\rho A}\right)/P$ is plotted against thrust in Fig. 14. Hover efficiency is much worse than climb efficiency, and the data fall into two distinct bands, as expected given the different airspeeds.
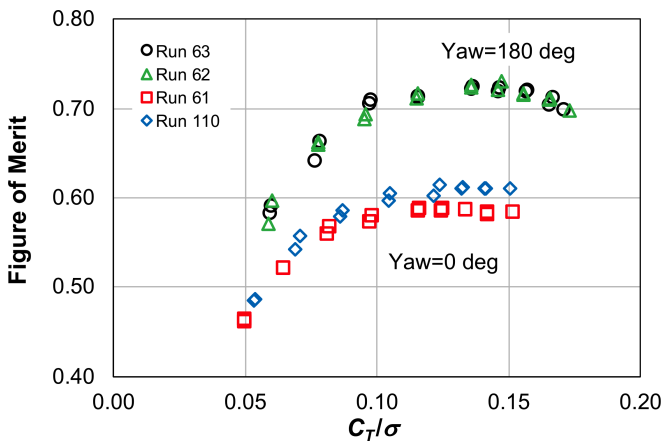
Fig. 14. Nominal Figure of Merit, M_{tip}=0.684.

Effects of Tip Speed

A few data runs were performed back-to-back at two different tip speeds, hover and airplane mode (M_{tip}=0.684 and 0.583, respectively). Example results are shown in Figs. 15 – 16, taken from Run 110, so the wind-tunnel configuration was exactly the same for both tip speeds. No hover/climb data were taken at M_{tip}=0.583 and at 180 deg yaw.

Figure 15 plots traditional power and thrust coefficients, which shows that the data are indeed comparable. To better

distinguish the effects of tip speed, Fig. 16 plots physical units, with shaft torque instead of power on the vertical scale, and Fig. 17 plots climb efficiency vs. thrust. It is evident that under these conditions, the higher tip speed gives better performance at high thrust, as expected. See the Airplane-Mode Data section for the effects of tip speed at high airspeed.
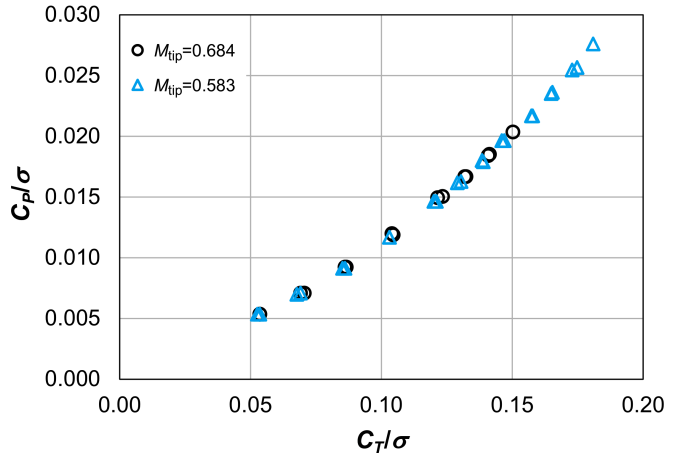
Fig. 15. Hover/climb power vs. thrust at two different tip speeds.
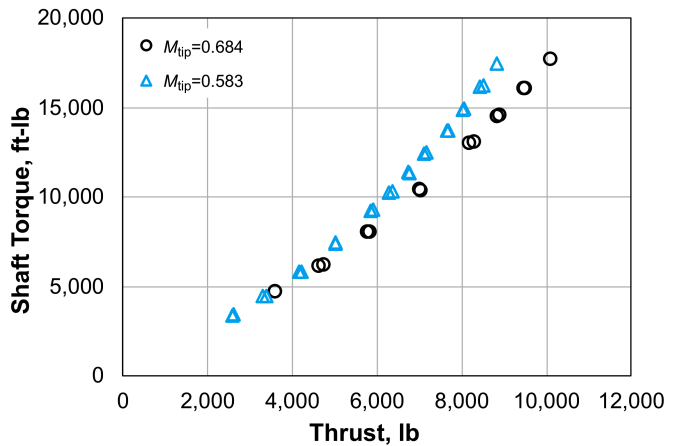
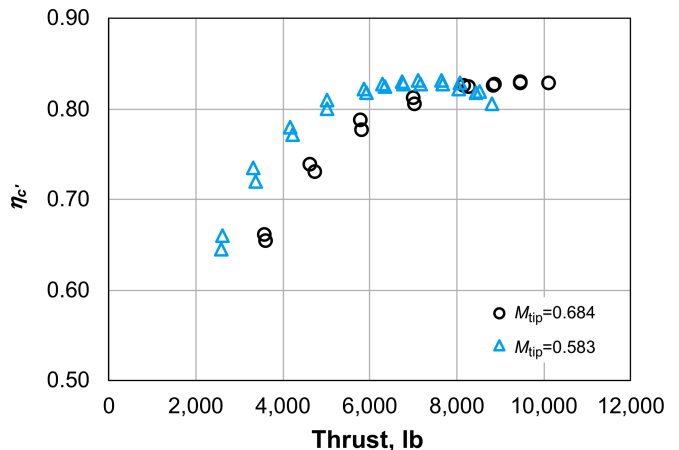**Fig. 16. Hover/climb torque vs. thrust at two different tip speeds.**

Fig. 17. Glauert-corrected climb efficiency η_c' vs. thrust at two different tip speeds.

11

Not all possible combinations of vane set positions and TTR orientation were tested. While it is possible that minor improvements in data range and quality could be obtained with further adjustments to the configuration, it would be more productive to do hover testing in the larger, 80-ft by120-ft test section. Furthermore, the differences between the data runs arise from the particulars of the wind-tunnel configuration, not from any problems with the TTR or rotor. The data shown here are more than sufficient to demonstrate the capability of the TTR to operate at near-hover conditions in the NFAC.

Conversion-Mode Data

This section presents thrust-sweep data at the conversion-mode test conditions in Fig. 8, preceded by an overview of key aerodynamic tare data.

Aerodynamic Tares

At high speed or high angle of attack, spinner loads can be a significant fraction of the total loads measured by the balance. Careful attention must therefore be paid to collecting good aerodynamic tare data for the spinner.

The process of determining spinner tares and other adjustments, such as the Glauert airspeed correction, over the entire range of airspeeds and yaw angles is iterative and remains a work in progress as of this writing. This section presents a sampling of spinner tare data to reveal the major issues, but does not attempt to give definitive results. Accordingly, the conversion-mode rotor data presented here are *not* corrected for spinner tares, wall effects, etc., and as such represent baseline data. The airplane-mode data were taken at higher dynamic pressures, so they were given very simple tare corrections as explained later in this paper. The hover/climb data were given no tare corrections because they were taken at very low dynamic pressure.

The TTR provides two sets of measurements to help determine spinner tares. These include direct measurement of spinner loads as well as rotor balance measurements. The spinner supports have strain gages to measure bending loads, hence spinner drag. The strain gages can collectively measure axial loads, but are poorly placed to measure transverse loads and moments. Spinner aerodynamic loads are usually at the extreme low end of the balance range, so balance accuracy (Table 9) can be a large fraction of the spinner tares.

The proper setup for measuring spinner tares poses a dilemma, in that neither a blades-off nor hub-off configuration can provide the exact flow conditions that would exist if the blades had no aerodynamic effect on the spinner. The hub yokes and bearings are covered by the blade roots, which act as aerodynamic fairings extending inside the spinner skirts. Removing the blades would expose the yokes to the flow and create high-drag conditions not present during normal operations. If instead the entire hub were to be removed, the effective area of the holes in the skirt fairing would be much larger than with blades installed, again resulting in non-representative flow conditions.

Given that there is no perfect way to acquire spinner tare data, an ideal spinner was simulated by removing the hub and blades and fairing over the skirt holes. This is the cleanest possible configuration, hence the lowest spinner drag. Figure 18 shows the fully-faired spinner and skirts at multiple yaw angles.

Fig. 18. Multiple exposure of spinner tare measurements, 0-100 deg yaw.

Although direct measurement of spinner loads by the internal strain gages would be ideal, the gages proved very sensitive to centrifugal loads and require recalibration under representative load conditions. Therefore, all aerodynamic tare data reported here were derived from the rotor balance.

Rotor balance data were acquired during yaw sweeps at seven different airspeeds (61 to 154 knots, q=12 to 75 lb/ft^2), and during fine yaw sweeps at three airspeeds (q=12, 36, and 75 lb/ft^2). All tare data shown here were taken at helicopter-mode shaft speed (569 rpm). The coarse yaw variations show consistent patterns of behavior at all airspeeds, but cannot properly capture the nonlinear behavior near 90 deg yaw. Therefore, tare corrections are best derived from the fine yaw data.

Figures 19-21 illustrate salient aspects of the spinner tares. A subset of data points is presented, chosen to include fine increments in yaw angle and consistent values of airspeed, given here as dynamic pressure q. Balance data are plotted as equivalent flat-plate area (load/q). The axis system is fixed to the balance and rotates with yaw angle. Note that in flight, the axis system is rotated so that the TTR "vertical" load becomes an outward side load, and the TTR "side" load here becomes a drag load.

For an idealized spinner, thrust would be slightly negative at zero yaw, transitioning to positive along a sine curve at high yaw angles. Figure 19 shows as much up to 90 deg, although the trend with q is inconsistent near zero yaw. The inconsistency is well within the accuracy of the measurement,

so is not of concern. However, there is clearly sharp drop in load just past 90 deg yaw, likely caused by separation.
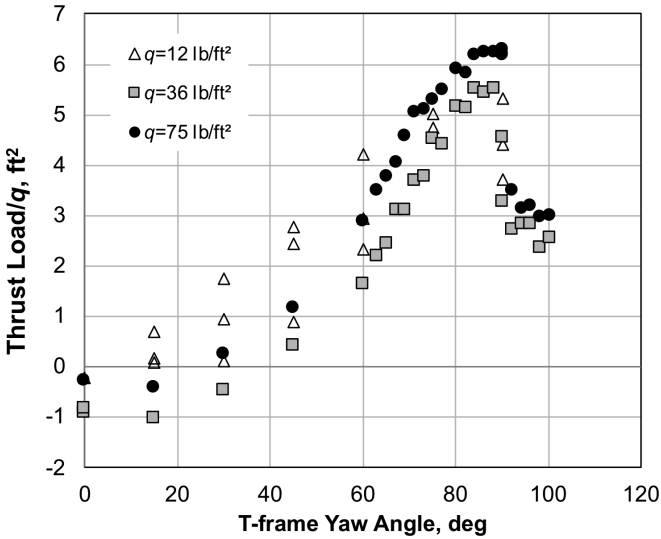

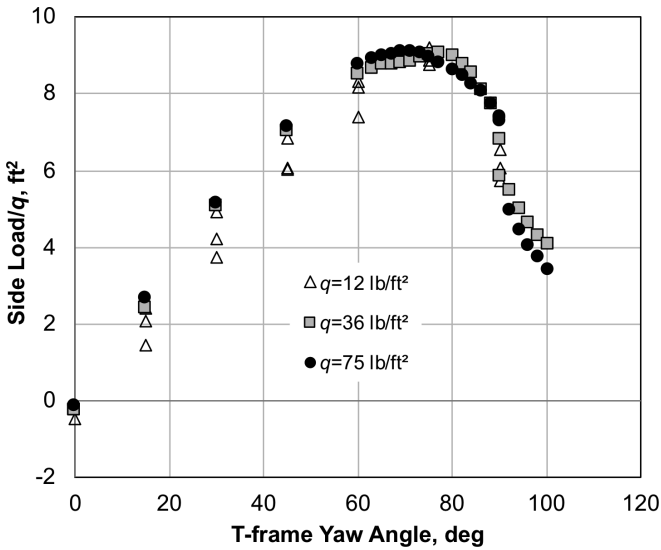**Fig. 19. Spinner thrust tare vs. yaw angle at three values of q.**

Fig. 20. Spinner side load tare vs. yaw angle at three values of q.

If the spinner were a perfect cylinder, the side load (parallel to the floor in Fig. 18) would follow a sine curve. Figure 20 shows an approximate sine trend, but with a peak value just above 70 deg, and a sharp drop above 90 deg. This trend is also consistent with stall/separation.

At the maximum value of thrust in Fig. 19, the equivalent C_L =1.12, based on the spinner base area. A hemisphere in a crossflow has an ideal $C_L = 0.69$ (Ref. 15), so a large forward thrust is within reason. Based on spinner drag at that data point (Fig. 20), $L/D<1$ as expected for an ellipsoidal spinner. These results are generally in keeping with those seen for the XV-15 spinner (Ref. 8, Figs. IV-7 and IV-8).
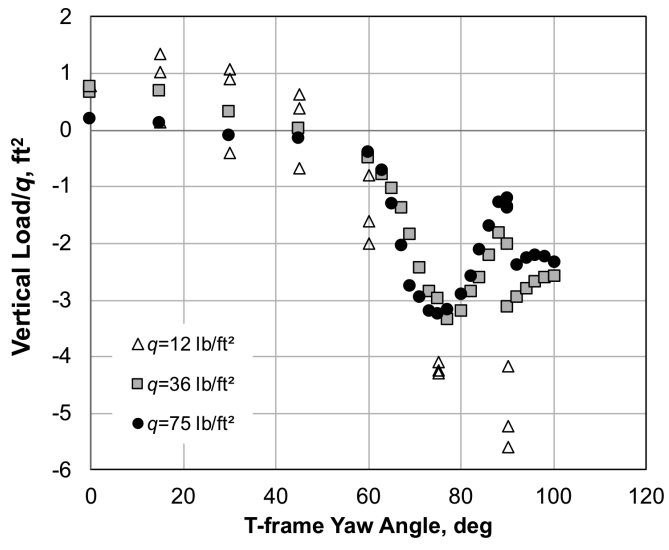
Fig. 21. Spinner vertical load vs. yaw angle at three values of q.

Finally, the spinner vertical load is plotted in Fig. 21. The strong, narrow peak near 75 deg is consistent with the Magnus effect; the peak is nearly eliminated at zero rotor speed (not shown). Again, there is a stall effect above 90 deg yaw. A brief test was performed with the hub installed but the blades and spinner hole covers removed. The Magnus effect was still present, so it cannot be assumed zero with the rotor installed.

In general, the trends of spinner load vs. yaw angle are more consistent at higher values of q. Side load has very consistent trends, even above 90 deg yaw (Fig. 20), whereas vertical load shows the least consistent behavior (Fig. 21).

Spinner tare data were also taken for pitch, roll and torque, the last as a check on instrumentation noise (the spinner torque should include only bearing drag, hence nearly zero). For brevity, those tare data are omitted here, but of course should be included in any analysis of the rotor data.

Conversion-Mode Rotor Data

Figures 23-26 present data for the conversion corridor: thrust sweeps for yaw variations (angle of attack sweep) at low speed, and for speed variations at fixed yaw angles.

Several thrust sweeps were performed at 58 knots, $\mu=0.125$, at different yaw angles from 70 to 100 deg. Resulting power vs. thrust data are shown in Fig. 22. Two separate thrust sweeps were performed at 90 deg yaw (helicopter mode); the data illustrate excellent repeatability. The plot reveals that power increases with decreasing nacelle angle, as expected.

Figures 22-26 show thrust sweeps at fixed yaw angles, 30, 45, 60 and 75 deg respectively (the horizontal rows in Fig. 8), for several different airspeeds from 58 to 160 knots ($\mu=0.125$ to 0.350). Note the changes in vertical scale for different yaw angles. For a given value of thrust, higher airspeed requires more power, again as expected.
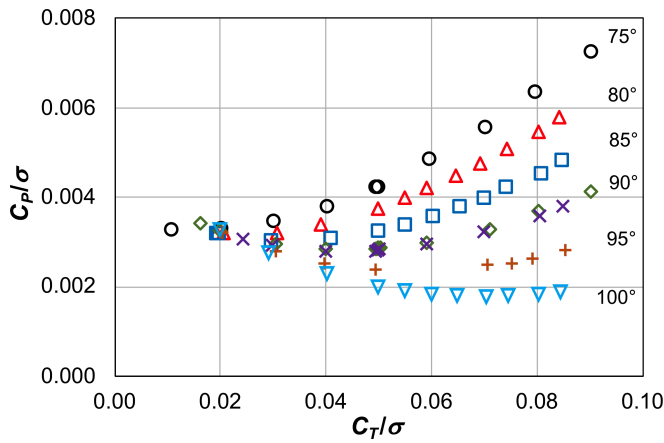
13

Fig. 22. Thrust sweeps from 75-100 deg yaw angle, M_{tip}=0.684, μ=0.125.
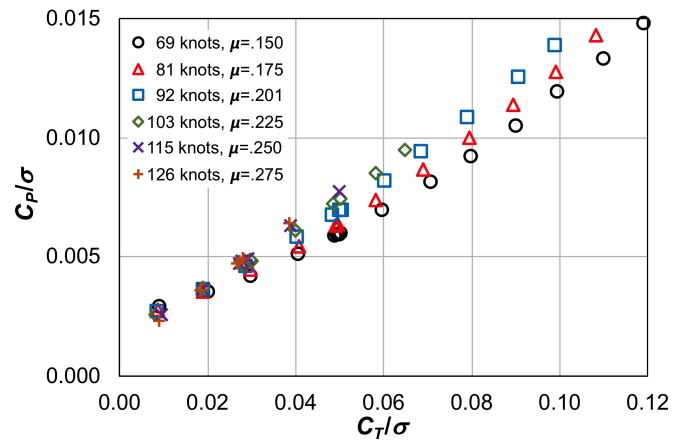

Fig. 25. Thrust sweeps from μ=0.150 to 0.275, 60 deg yaw angle, M_{tip}=0.684.
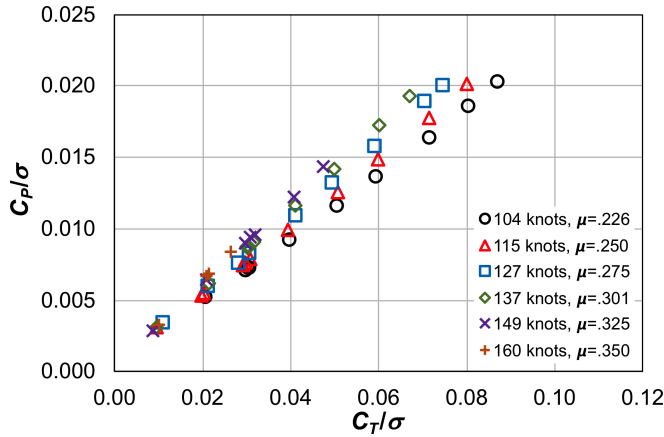

Fig. 23. Thrust sweeps from μ=0.226 to 0.350, 30 deg yaw angle, M_{tip}=0.684.
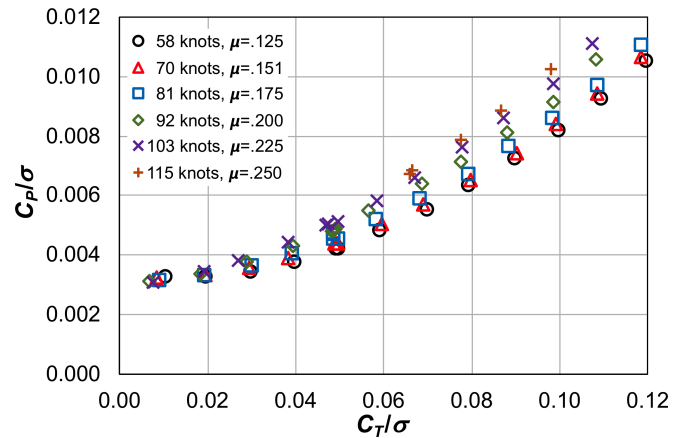

Fig. 26. Thrust sweeps from μ=0.125 to 0.250, 75 deg yaw angle, M_{tip}=0.684.
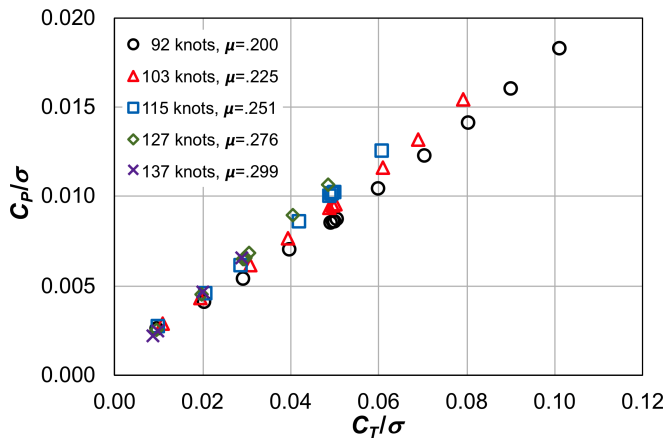
Airplane-Mode Data

During airplane-mode testing, the rotor speed was set to either M_{tip}=0.583, the nominal cruise value, or to M_{tip}=0.684, the helicopter-mode value. Nominal tip speeds were 651 and 775 ft/sec, respectively. In normal tiltrotor operations, the rotor speed is held to the higher value until conversion to airplane mode is complete, then the rotor is slowed to the lower value before accelerating to full cruise speed. Wind tunnel airspeed was set by advance ratio, so airspeed varied with both tip speed and temperature. Thrust sweeps were performed at each combination of tip Mach number and advance ratio.

The TTR checkout test acquired most of the airplane-mode data at M_{tip}=0.583, but as many test conditions as possible were matched at helicopter tip speed for comparison.

In airplane mode, the only aerodynamic tare is spinner drag. Because of the higher range of airspeeds compared to conversion mode, the drag tare was determined separately from conversion mode (previous section). The maximum airspeed reached during the tare measurements was 275 knots.

Fig. 24. Thrust sweeps from μ=0.200 to 0.299, 45 deg yaw angle, M_{tip}=0.684.

14

All airplane-mode rotor data in this section are corrected for spinner drag derived from the rotor balance data and linear trend in Fig. 27. The spinner drag is at the lower end of the useable range of the rotor balance; the maximum drag measured (168 lb) was barely more than 1% of the calibrated range (Table 9), or 0.5% of maximum capability (Table 2). There is clearly hysteresis, but the linear trend is obvious. The equivalent flat plate area of the 699 spinner at 0 deg yaw is 0.669 ft^2, which is slightly lower than the value measured for the XV-15 spinner (Ref. 8).
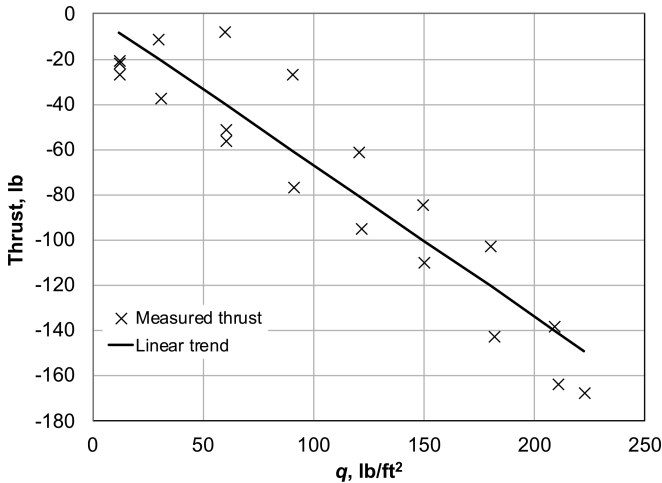
Fig. 27. Spinner drag in airplane mode.

The measured value of spinner drag based on balance data would ideally be replaced with directly measured values of spinner drag, based on the spinner strain gages. The strain gages are better matched to the range of spinner drag and should be more accurate than the balance over that range. However, the gages are sensitive to centrifugal loads and require recalibration, so their data are not used here.

Prior to the TTR/699 test, the most extensive high-speed, full-scale proprotor tests were of the XV-15 and JVX rotors (Refs. 8, 9 and 16). The XV-15 rotor was tested on the Propeller Test Rig (Fig. 28), whereas the JVX rotor was tested on the Prop Test Rig (Fig. 29). Data from those tests are briefly summarized here to illustrate the advancement of TTR over previous state of the art, although no detailed comparisons are offered.

Figures 30 and 31 show the TTR/699 data at airplane mode tip speed in physical units and as rotor performance coefficients, respectively. For both figures, the rotor was set to $M_{tip} = 0.583$. Neither the XV-15 nor JVX rotor data were taken at consistent values of M_{tip}, or even at consistent advance ratios for the XV-15. Therefore, those data sets are represented by outlines of the test conditions achieved without identifying individual data points. It is immediately evident that the TTR checkout test achieved a major increase in capability. Moreover, the eight TTR/699 trendlines taken together constitute a much more comprehensive data set than previously available.

Fig. 28. XV-15 rotor on the Propeller Test Rig (1970).

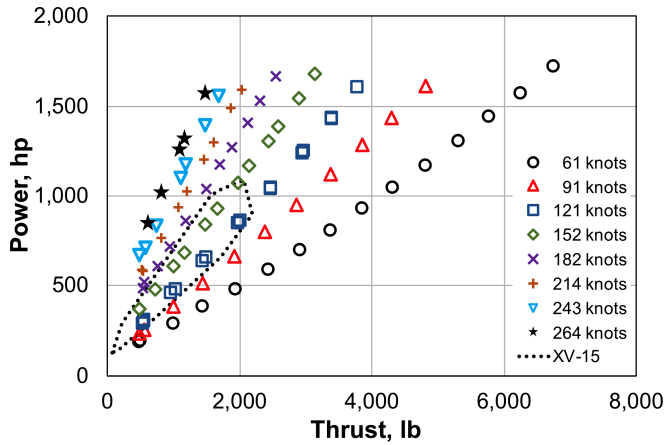**Fig. 29. Scaled JVX rotor on the Prop Test Rig (1991).**

15

Fig. 30. TTR/699 thrust sweeps at M_{tip}=0.583, compared to XV-15 data limits.
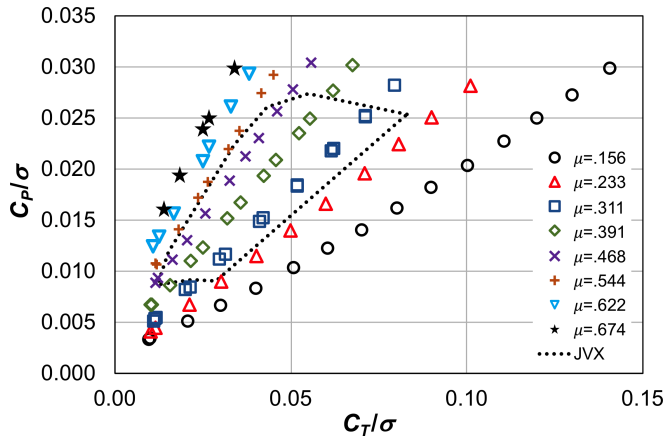

Fig. 31. TTR/699 thrust sweeps at M_{tip}=0.583, compared to JVX data limits.

Figure 32 plots propulsive efficiency η versus thrust. Plotted at nominal C_T/σ, the data points strongly overlap and are difficult to distinguish. In Fig. 33, the leftmost set of values, at 264 knots, is plotted at nominal C_T/σ, but the other data points are offset in increments of +0.02 C_T/σ moving rightwards, thus revealing each trend. Propulsive efficiency peaks near C_T/σ =0.08. However this value of η occurs at a much higher value of thrust (3,900 lb) and at lower airspeed (122 knots) than typical for cruising flight. Indeed, the aircraft would be near stall under these conditions (see the conversion envelope, Fig. 8). Propulsive efficiency at high airspeed and low thrust may not appear to be as impressive as the peak value, but it is in fact much more important for aircraft and rotor design.

In this paper, the Glauert correction is applied to propulsive efficiency, but not to the nominal test section velocities listed on the figure legends. In normal NFAC operations, the rotor advance ratio is based on the uncorrected airspeed and the data are so stored in the database. Higher-order corrections for wall effects, blockage, etc. are possible, so the airspeed correction of equation (3) is not definitive.
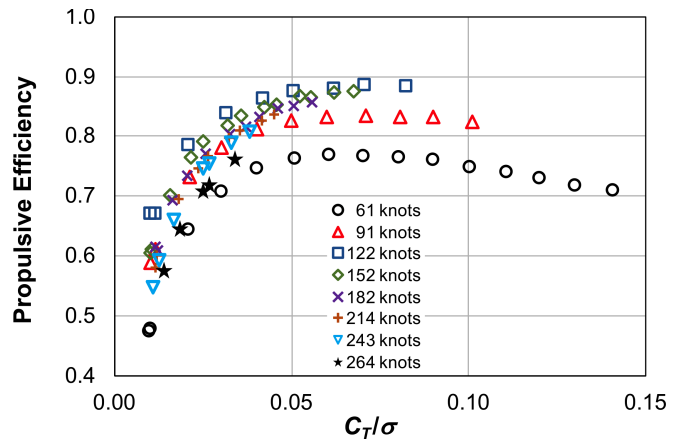

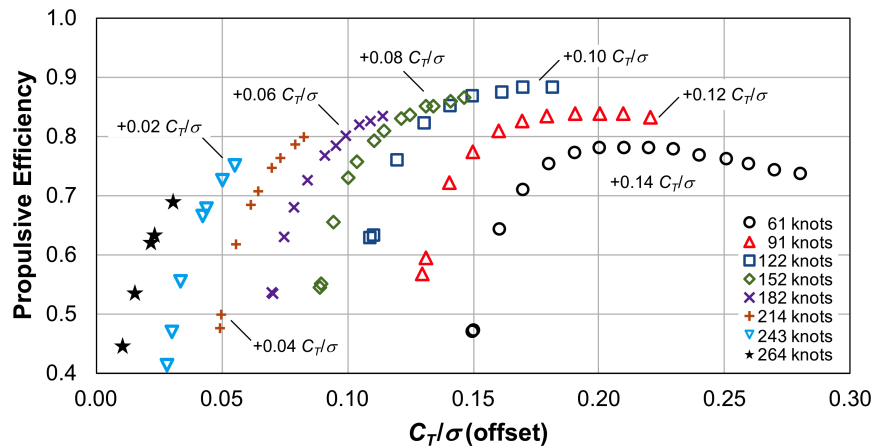**Fig. 32. TTR/699 propulsive efficiency at M_{tip}=0.583.**

Fig. 33. TTR/699 propulsive efficiency at M_{tip}=0.583. Each speed is offset by C_T/σ=+0.02.

16

Figures 34 and 35 show data taken at helicopter-mode tip speed, $M_{tip}=0.684$. Figure 34 shows data in physical units to better reveal the effects of tip speed (compare Fig. 30). At a given airspeed, the higher tip speed achieved slightly higher values of thrust, but at the cost of higher power at high airspeeds. Compare, for example the values of thrust and power at 61 knots, which are closely matched at 6,000 lb thrust and 1,500 hp (Fig. 30 vs. Fig. 34). However, at 212-214 knots and 2,000 lb thrust, the power at $M_{tip}=0.684$ is higher than at $M_{tip}=0.583$. The difference may appear small at the scale of Figs. 30 and 34, or Figs. 31 and 35, but it translates into an improvement in propulsive efficiency of 5% at 2000 lb thrust, rising to 12% at 750 lb thrust, a value more typical of trimmed flight (Fig. 36).
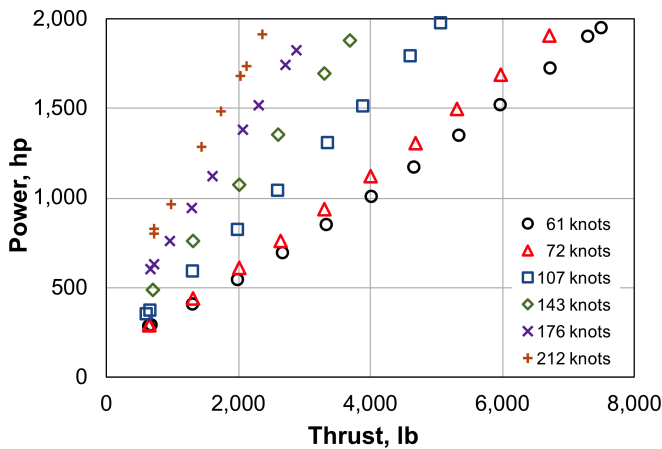

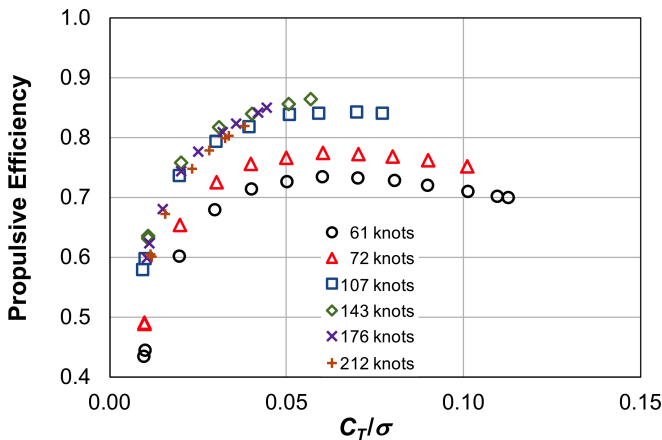
Fig. 34. TTR/699 thrust sweeps at $M_{tip}=0.684$.

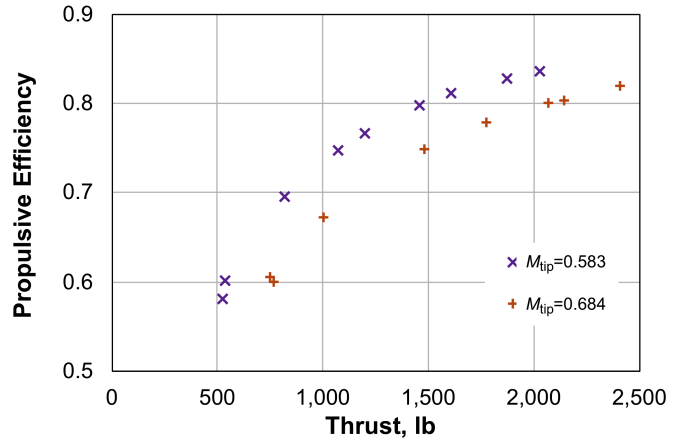**Fig. 35. TTR/699 propulsive efficiency at $M_{tip}=0.684$.**

Fig. 36. TTR/699 propulsive efficiency at $M_{tip}=0.684$ vs. $M_{tip}=0.583$, 212-214 knots.

FUTURE WORK

It is planned to make the TTR/699 database available to the research community. The most important remaining task is to ensure that all known corrections for thermal effects, balance interactions, etc. have been consistently applied to all measurements. Aerodynamic tares will also be applied throughout, along with basic corrections for wall effects. The database will include data with and without corrections, so that researchers can develop alternative corrections if desired. Extending the work of Ref. 17 to include the 699 rotor is an obvious recommendation.

It should be possible to replace spinner aerodynamic tares, at least in the thrust/drag axis, with direct measurements of spinner loads. The raw data require correction for centrifugal effects, which in turn require recalibration of the spinner strain gages.

Looking beyond the existing data, there are many possibilities for future testing of the TTR. Upgrading the NFAC fan drives and adding strut fairings would increase the maximum airspeed. A glance at Fig. 8 will suggest several opportunities for additional flight conditions both within and beyond the nominal conversion corridor. Testing the TTR in the 80x120 test section would more closely approach true hover, and should give better quality data in helicopter and conversion modes due to reduced wall effects. In principal, the 80x120 test section could be used to simulate vortex ring state conditions.

An upgraded rotor control system would permit operations at higher rotor loads, hence higher thrust, which would expand the test envelope at low speeds. TTR control-system loads are limited by a very few components, so improvements should be straightforward, given that the actual loads are now better understood.

17

Given that a wind-tunnel test has no need to trim an aircraft or keep within the operating limits of the aircraft engine or gearbox, it may be possible to further reduce the 699 rotor tip speed in airplane mode, although load limits would be expected to constrain the safe operating envelope.

CONCLUSIONS

The Tiltrotor Test Rig completed its first wind-tunnel entry in November 2018. The Bell Model 699 research rotor was installed for the test. Testing included a total of 1554 rotor data points at 60 combinations of rotor tip speed, yaw angle, and tunnel speed, reaching a maximum airspeed of 273 knots. Specific accomplishments include:

1. Acquired detailed airplane-mode performance data at two tip speeds (airplane and helicopter) and eight airspeeds, from 61 to 264 knots.
2. Acquired conversion-mode performance data at 29 combinations of airspeed and nacelle angle, up to 160 knots.
3. Acquired baseline hover (wind-off) data in upstream & downstream orientations (equivalent to low-speed vertical climb), including thrust sweeps at two tip speeds and rotor speed (rpm) sweeps.
4. Acquired acoustics reference data at all test points, including dedicated thrust and yaw sweeps.
5. Acquired control-response data at selected test points.
6. Acquired extensive spinner tare data throughout the flight envelope.
7. Evaluated TTR drive-motor power when connected to the NFAC motor-generator set.
8. Demonstrated good TTR motor and drive-train thermal control throughout the operating range.

Taken together, these accomplishments thoroughly demonstrated the capability of the TTR up to the limits of the NFAC operating envelope while providing a comprehensive database of benchmark rotor data. The test also identified upgrades to improve productivity and extend the test envelope to support future rotor testing.

The TTR/699 test generated an unprecedented collection of full-scale proprotor performance, loads and acoustics data, constituting a major advancement over previous testing capability.

Author contacts:

C. W. Acree, cecil.w.acree@nasa.gov
A. L. Sheikman, alex.l.sheikman@nasa.gov
T. R. Norman, tom.norman@nasa.gov

REFERENCES

1. Acree, C. W., Jr., and Sheikman, A. L., "Development and Initial Testing of the Tiltrotor Test Rig." American Helicopter Society 74th Annual Forum Proceedings, Phoenix, AZ, May 2018.

2. Kottapalli, S. and Acree, C. W., "Correlation of Full-Scale Isolated Proprotor Performance and Loads," Vertical Flight Society 75th Annual Forum Proceedings, Philadelphia, PA, May 2019.

3. Schatzman, N. L. and Malpica, C., "Acoustic Testing of the Tiltrotor Test Rig in the National Full-Scale Aerodynamics Complex 40- by 80-FootWind Tunnel," Vertical Flight Society's 75th Annual Forum Proceedings, Philadelphia, PA, May 2019.

4. Solis, E., and Meyn, L., "Photogrammetric Deflection Measurements for the Tiltrotor Test Rig (TTR) Multi-Component Rotor Balance Calibration," American Helicopter Society Technical Meeting on Aeromechanics Design for Vertical Lift Proceedings, San Francisco, California, January 2016.

5. Russell, C. R., and Acree, C. W., "Modal Test and Analysis of the NASA Tiltrotor Test Rig," American Helicopter Society Technical Conference on Aeromechanics Design for Transformative Vertical Lift Proceedings, San Francisco, CA, January 2018.

6. Kottapalli, S., and Acree, C. W., "Analytical Performance, Loads, and Aeroelastic Stability of a Full-Scale Isolated Proprotor," American Helicopter Society Technical Conference on Aeromechanics Design for Transformative Vertical Lift Proceedings, San Francisco, CA, January 2018.

7. Kottapalli, S., Russell, C. R., Acree, C. W., and Norman, T.R., "Aeroelastic Stability Analysis of a Full-Scale Isolated Proprotor on the Tiltrotor Test Rig," Dynamics Specialists Conference, AIAA SciTech Forum Proceedings, San Diego, CA, January 2019.

8. Bell Helicopter Company, "Advancement of Proprotor Technology. Task II – Wind-Tunnel Test Results," NASA CR-114363, Bell Report 300-099-004, September 1971.

9. Felker, F. F., "Results from a Test of a 2/3-Scale V-22 Rotor and Wing in the 40- by 80-Foot Wind Tunnel," American Helicopter Society 47th Annual Forum Proceedings, Phoenix, Arizona, May 1991.

10. van Aken, J. and Yang, L, "Development of a new State-of-the-Art Data Acquisition System for the National Full-Scale Aerodynamics Complex Wind Tunnels," AIAA-2009-1346, 47th AIAA Aerospace Sciences Meeting Proceedings, Orlando, FL, January 2009.

11. Harris, J. C., Scheidler, P.F, Hopkins, R, and Fortenbaugh, R.L., "Initial Power-Off Testing of the BA609 Tiltrotor," American Helicopter Society 66th Annual Forum Proceedings, Phoenix, AZ, May 2010.

12. Johnson, W., *Rotorcraft Aeromechanics*, Cambridge University Press, 2013.

13. Glauert, H., *The Elements of Aerofoil and Airscrew Theory*, Chap. XVII, pp. 222–226, Cambridge University Press, 2nd Ed., 1947.

14. Pope, A. and Harper, J. J., *Low-Speed Wind Tunnel Testing*, pp. 362–364, John Wiley and Sons, 1966.

15. McKinley, G., "MIT2_25F13_Solution6.8," MIT OpenCourseWare, dated March 31, 2015, http://ocw.mit.edu (accessed May 2, 2015).

16. Acree, C. W., "Assessment of JVX Proprotor Performance Data in Hover and Airplane-Mode Flight Conditions," NASA/TM-2016-219070, February 2016.

17. Koning, W. J. F., "Wind Tunnel Interference Effects on Tiltrotor Testing Using Computational Fluid Dynamics," NASA CR-2016-219086, March 2016.